Article

Janus graphene nanoribbons with localized states on a single zigzag edge

https://doi.org/10.1038/s41586-024-08296-x

Received: 17 April 2024

Accepted: 28 October 2024

Published online: 8 January 2025

Check for updates

Shaotang Song[1,8], Yu Teng[1,2,8], Weichen Tang[3,4,8], Zhen Xu[5,8], Yuanyuan He[1], Jiawei Ruan[3,4], Takahiro Kojima[5], Wenping Hu[2,6], Franz J. Giessibl[7], Hiroshi Sakaguchi[5]✉, Steven G. Louie[3,4]✉ & Jiong Lu[1]✉

Topological design of π electrons in zigzag-edged graphene nanoribbons (ZGNRs) leads to a wealth of magnetic quantum phenomena and exotic quantum phases[1–10]. Symmetric ZGNRs typically show antiferromagnetically coupled spin-ordered edge states[1,2]. Eliminating cross-edge magnetic coupling in ZGNRs not only enables the realization of a class of ferromagnetic quantum spin chains[11], enabling the exploration of quantum spin physics and entanglement of multiple qubits in the one-dimensional limit[3,12], but also establishes a long-sought-after carbon-based ferromagnetic transport channel, pivotal for ultimate scaling of GNR-based quantum electronics[1–3,9,13]. Here we report a general approach for designing and fabricating such ferromagnetic GNRs in the form of Janus GNRs (JGNRs) with two distinct edge configurations. Guided by Lieb's theorem and topological classification theory[14–16], we devised two JGNRs by asymmetrically introducing a topological defect array of benzene motifs to one zigzag edge, while keeping the opposing zigzag edge unchanged. This breaks the structural symmetry and creates a sublattice imbalance within each unit cell, initiating a spin-symmetry breaking. Three Z-shaped precursors are designed to fabricate one parent ZGNR and two JGNRs with an optimal lattice spacing of the defect array for a complete quench of the magnetic edge states at the 'defective' edge. Characterization by scanning probe microscopy and spectroscopy and first-principles density functional theory confirms the successful fabrication of JGNRs with a ferromagnetic ground-state localized along the pristine zigzag edge.

The term 'Janus' has been adopted to denote materials that show different properties on two opposing sides or faces[17,18]. In the realm of two-dimensional materials, creating asymmetric Janus materials by breaking the top- and bottom-layer symmetry provides an attractive route for engineering properties and functionalities such as enhanced valley spin splitting, out-of-plane piezoelectricity and second harmonic generation[19–22]. Reducing the dimension of Janus materials from two-dimensional to one-dimensional systems with two different edge structures or topologies (hence properties), especially those with an asymmetric zigzag edge in Janus zigzag-edged graphene nanoribbons (JGNRs), creates opportunities for the realization of one-dimensional ferromagnetic quantum spin chains and the assembly of multiple qubits. It also enables the creation of ferromagnetic transport channel in the one-dimensional limit[23,24], which can carry completely spin-polarized current without applying an in-plane electric field[10], strain[25] or chemical functionalizations[26,27], as required for conventional zigzag-edged graphene nanoribbons (ZGNRs).

Although theoretical attempts have been made to break the zigzag structural symmetry by attaching triangular fragments to one edge of the ZGNRs, the resulting ferromagnetic state is more delocalized and extends into the triangular fragments[28]. Moreover, the experimental realization of such GNRs remains elusive, as the rational design of precursors towards such GNRs requires the simultaneous breaking of their structural and spin symmetries. This task is even more challenging than fabricating symmetric ZGNRs, which is notoriously difficult owing to their high reactivity and the challenges in the design and synthesis of precursors. So far, only two symmetric ZGNRs have been reported, both based on the U-shaped precursor design. Moreover, the width of the obtained ZGNRs is limited to having six carbon zigzag chains across the ribbon, namely, 6-ZGNR[1,2].

The design principle for JGNRs

Guided by topological considerations, our strategy for creating such JGNRs involves decorating one zigzag edge with a topological 'defect' array (termed as the TDZ edge), while keeping the other zigzag edge unchanged. We introduce a periodic array of benzene motifs attached to the TDZ edge to break structural symmetry and to create a sublattice imbalance ($\Delta N = 1$), leaving one net unpaired site in each unit cell[14,29] (Fig. 1a). As a result, this introduces a zero-energy band in line with

[1]Department of Chemistry, National University of Singapore, Singapore, Singapore. [2]Joint School of National University of Singapore and Tianjin University, International Campus of Tianjin University, Fuzhou, China. [3]Department of Physics, University of California, Berkeley, Berkeley, CA, USA. [4]Materials Sciences Division, Lawrence Berkeley National Laboratory, Berkeley, CA, USA. [5]Institute of Advanced Energy, Kyoto University, Kyoto, Japan. [6]Tianjin Key Laboratory of Molecular Optoelectronics, Department of Chemistry, School of Science, Tianjin University, Tianjin, China. [7]Institute of Experimental and Applied Physics, University of Regensburg, Regensburg, Germany. [8]These authors contributed equally: Shaotang Song, Yu Teng, Weichen Tang, Zhen Xu. ✉e-mail: sakaguchi@iae.kyoto-u.ac.jp; sglouie@berkeley.edu; chmluj@nus.edu.sg

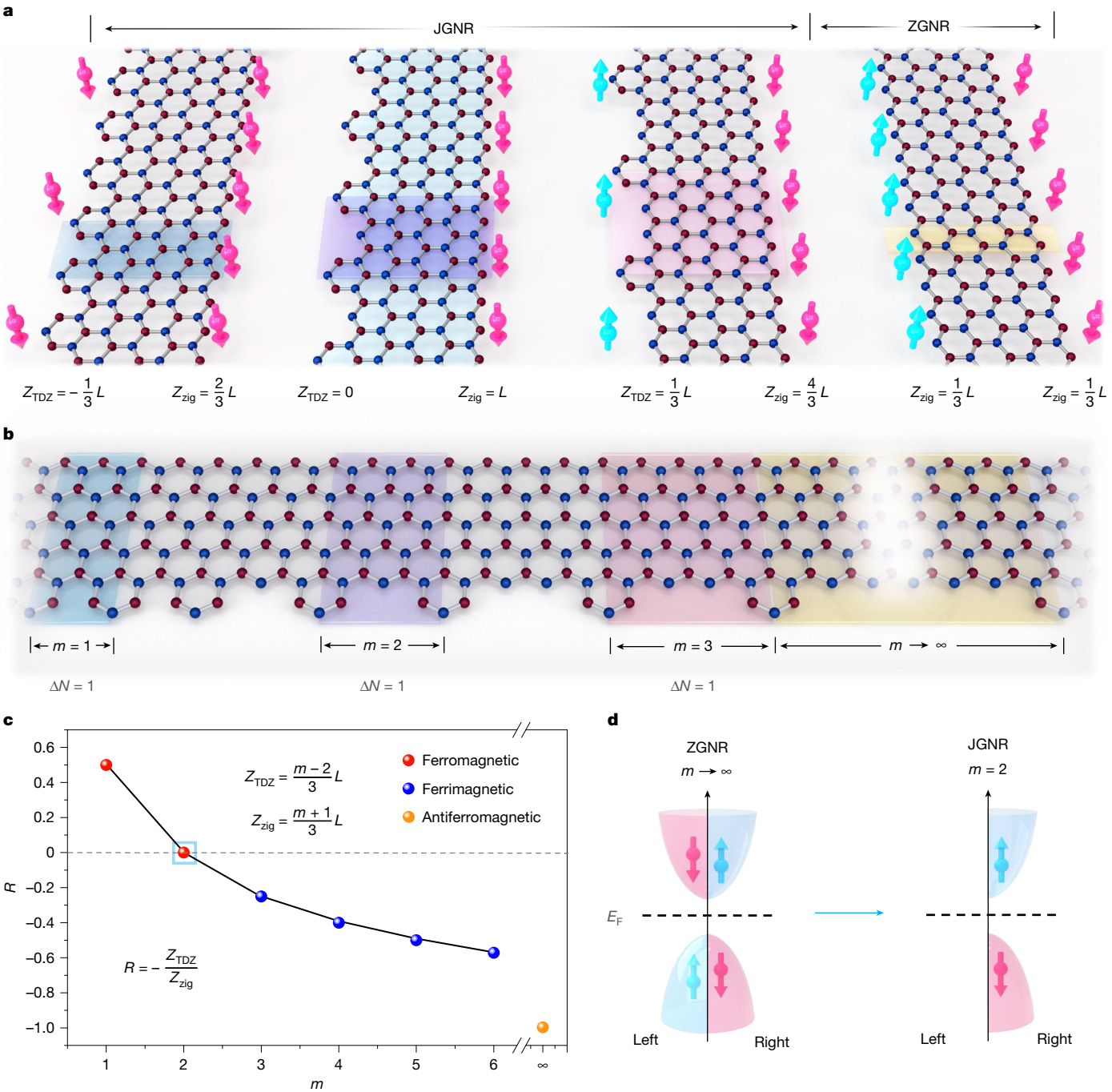

Fig. 1 | Design principle of JGNRs. a, Schematic illustration of JGNRs with various TDZ edges of different m values. The red and blue arrows represent spin-up and spin-down of edge states (by convention), respectively. The numbers at the bottom represent the CPI index of the corresponding TDZ (Z_{TDZ}) and intact zigzag (Z_{zig}) edges, where L is the number of unit cells for a finite-length ribbon along the zigzag direction (the unit cells are shaded by colours). The red and blue atoms are carbon atoms from two different sublattices. **b**, Schematic diagram of the repeated unit of JGNRs, illustrating a gradual increase in 'defective' site spacing between adjacent benzene rings, progressing from left to right: 1, 2, 3 and towards infinity (∞). The sublattice imbalance per unit cell remains as $\Delta N = 1$ for all the cases except for $m = \infty$. **c**, The m-dependent magnetic orderings between the two edges, which can be described using the negative sign of the ratio of the CPI index for the two edges of JGNRs (defined as $R = -(Z_{TDZ}/Z_{zig})$). As m increases, R transforms from a positive to a negative value, crossing 0 at $m = 2$. From Lieb's theorem and CPI theory, a JGNR undergoes a transition from ferromagnetic to antiferromagnetic through a region of ferrimagnetic coupling. **d**, Schematic diagram of the spin-polarized band structure near the fundamental bandgap going from ZGNR ($m = \infty$, antiferromagnetic coupling between the two symmetric zigzag edges that are ferromagnetically ordered) to JGNR ($m = 2$, ferromagnetic order at only the single zigzag edge).

Lieb's theorem, initiating the spin-symmetry breaking[30–32]. To effectively quench the spin polarization at the TDZ edge and maintain a singly occupied ferromagnetic edge-state band at the zigzag edge, the key is to determine the optimal spacing (denoted as m, $m = 1$, $m = 2$, $m = 3$ and so on) between periodic benzene rings at the TDZ edge that maximally disrupts the edge states. To achieve this, we applied the topological classification theory using chiral symmetry developed in ref. 16. In one-dimensional bipartite lattices such as GNRs, because of the negligible second-nearest-neighbour interactions, chiral symmetry is well satisfied, leading to a Z-classification of electronic topological

phases with a conventional Z index[16]. As the Z index is zero for a vacuum (which is a topological trivial phase), the count of end states can be deduced from the Z index of the GNRs.

Here we use an important correspondence that the edge of a JGNR (which can be either a defective zigzag edge or a normal zigzag edge) can be viewed as the end of a wide armchair-edged GNR (AGNR) in the large-width limit (Extended Data Fig. 1). This means that the topological edge states of a defective zigzag edge are the topological end states of a large-width AGNR with the same defective structure at its end. For the end of an AGNR, the Z index is given by[16]:

$$Z = W_{\mathrm{notco}} - \left\lfloor \frac{W}{3} \right\rfloor \quad (1)$$

where W is the number of rows of carbon atoms forming its width, and W_{notco} is the number of rows of atoms with unconnected carbon pairs within the specific unit cell that is commensurate to the end termination. The topless brackets denote mathematically the floor function.

Figure 1a shows a family of JGNRs with different spacing of m as defined in Fig. 1b. We map the edge of a finite-length JGNR to the end of a large-width AGNR with the same structure. For a JGNR consisting of L unit cells along the defect zigzag edge direction, the associated AGNR will contain L repeat units along the width of AGNR (with L taken in the large limit and equal to a multiple integer of 3). The number of rows of carbon atoms forming the width of the AGNR is $W = 2(m+1)L$, where m is the number of missing benzene rings, as shown in Fig. 1a. For the TDZ edge of the JGNR, $W_{\mathrm{notco}} = mL$, and the corresponding chiral phase index (CPI; which dictates the number of topological edge states) is $Z_{\mathrm{TDZ}} = \frac{m-2}{3}L$ using the Jiang–Louie formula[16] given in equation (1). For the non-defective edge, the width of the associated AGNR is the same $W = 2(m+1)L$, whereas $W_{\mathrm{notco}} = (m+1)L$, and the corresponding CPI is $Z_{\mathrm{zig}} = \frac{m+1}{3}L$ (Extended Data Fig. 2). Moreover, to account for the spin degree of freedom, Lieb's theorem is applied, leading to spin-polarized topological edge states and a magnetic ground state. As illustrated in Fig. 1b, the sublattice imbalance for all JGNRs is $\Delta N = L$ (as the sublattice imbalance per unit cell is $\Delta N = 1$). Thus, the ground state consists of $\frac{m-2}{3}L$ spin-up (by convention and a negative Z_{TDZ} denotes a reversal of spin orientation) topological states localized at the TDZ edge of JGNRs and $\frac{m+1}{3}L$ spin-down topological states localized at the regular zigzag edge. Our ab initio density functional theory (DFT) calculations numerically validated these topological findings (Supplementary Figs. 1 and 2).

With the CPI analysis and the Jiang–Louie formula, we reach the following prediction without using any detailed calculations. The sign of the quantity R, defined as the negative of the ratio between the CPI of the two edges $R = -(Z_{\mathrm{TDZ}}/Z_{\mathrm{zig}}) = -((m-2)/(m+1))$, determines the magnetic ordering of the JGNRs (Fig. 1c). For $m = 1$ (with $R > 0$), both edges of the JGNR have the same spin alignment but with different magnitude, giving rise to a ferromagnetic state. In contrast, for $m > 2$ (where $-1 < R < 0$), the two edges of the JGNR show different spin configurations with varying magnitude, resulting in a ferrimagnetic order. Notably, when $m = 2$ ($R = 0$), no edge state exists at the TDZ edge, leading to a ferromagnetic ground state localized exclusively at the zigzag edge. The band structure near the Fermi level (E_{F}) for the $m = 2$ case (Fig. 1d) is in marked contrast to that of the symmetric ZGNRs with antiferromagnetically coupled edge states. The symmetric ZGNRs can be viewed as an extreme scenario with $m = \infty$ (with $R = -1$), where the perturbation of the infinitely spaced benzene rings becomes 0. Therefore, by varying the parameter m, our theory predicts the emergence of different magnetic ground states with different cross-edge couplings in JGNR, which is unattainable in symmetric ZGNRs (Fig. 1a). Below, we used the notation (n,m)-JGNRs to describe the specific JGNRs, where n refers to the number of carbon zigzag chain laterally across the ribbon and m denotes the benzene ring spacing at the TDZ edge.

Precursor design for on-surface synthesis of JGNRs

To achieve the on-surface synthesis of two JGNRs (with $n = 4$ and $n = 5$, $m = 2$), we use a Z-shaped precursor design for the asymmetric fabrication, in contrast to the U-shaped design for the synthesis of 6-ZGNRs[33–36]. The Z-shaped precursor comprises two independent branches that are interconnected by a carbon–carbon (C–C) bond (Fig. 2). At the termini of the branches, two bromine (Br) atoms are installed as connection sites for thermally induced aryl–aryl coupling. This design allows for the independent modification of individual branches for the separated control over the edge geometries of the resulting JGNRs. Utilizing methylphenanthrene groups for both branches (precursor **3** in Fig. 3) yields two identical zigzag edges, corresponding to the 5-ZGNR. Intriguingly, substituting one of the methylphenanthrene groups with an oligophenyl group results in the modification of one of the zigzag edges to our target TDZ edge with periodically decorated benzene rings (with a spacing of $m = 2$). In addition, adjusting the length of the oligophenyl groups from biphenyl to triphenyl (precursors **1** and **2** in Fig. 2) enables the modulation of the width of the JGNRs from $n = 4$ to $n = 5$.

The precursors were successfully obtained via multi-step organic synthesis (Supplementary Information) and then separately deposited onto a clean Au(111) surface under ultrahigh vacuum. Stepwise annealing of the precursor decorated surfaces induces polymerization and cyclodehydrogenation reactions to yield the corresponding (4,2)- and (5,2)-JGNRs (Fig. 2) and 5-ZGNR (Fig. 3). The topographic scanning tunnelling microscopy (STM) images of both JGNRs reveal bright lobes at the intact zigzag edge and larger protrusions at the TDZ edges, corresponding to the position of periodically spaced benzene rings (Fig. 2b,d). The bond-resolved STM (BR-STM) images of both JGNRs acquired at −10 mV using a carbon monoxide (CO)-functionalized tip show the corrugated hexagon-like rings in the centre and distorted lobe features along the edges, which are presumably attributed to the perturbations induced by the electronic states of the JGNRs in the vicinity of the Fermi level (E_{F})[37,38] (Fig. 2c,e). In contrast, the BR-STM image of 5-ZGNR acquired at 10 mV clearly resolves the characteristic hexagon patterns of the backbone, indicating an absence of electronic states near E_{F} (Fig. 3j). In addition, non-contact atomic force microscopy (nc-AFM) images directly confirm the different edge morphologies of the expected JGNRs as defined by the precursor design.

Scanning tunnelling spectroscopy of the GNRs

Previous studies have shown that magnetic edge states cannot be directly observed in the wider pristine 6-ZGNR and N-doped 6-ZGNR, because they couple strongly to the metal substrate[1,2]. Compared with 6-ZGNR, both 5-ZGNR and two JGNRs have a narrower ribbon width, thus leading to a more rigid backbone that could prevent strong structural downwards bending and electronic coupling with the substrate[39]. Our differential conductance ($\mathrm{d}I/\mathrm{d}V$, where I and V represent the tunnelling current and bias voltage, respectively) spectroscopic measurements acquired over both 5-ZGNR and JGNRs confirm that magnetic edge states, predicted by gas-phase theoretical calculations, can survive on Au(111). The $\mathrm{d}I/\mathrm{d}V$ spectrum obtained at the edge of 5-ZGNR shows 3 distinct peaks located at 760 ± 18 mV (peak A), −300 ± 5 mV (peak B) and −410 ± 7 mV (peak C), yielding an apparent bandgap of $\Delta E_{\mathrm{exp}} = 1{,}060 \pm 19$ meV (Fig. 3c and Extended Data Fig. 4c,d). Our experimental gap of 5-ZGNR is smaller than that of the 6-ZGNR (1.5 eV) on a monolayer NaCl island[1]. Such behaviour is probably owing to the screening effect of the metal substrate in reducing the quasiparticle energies and bandgaps of reduced dimensional systems[40–43]. The $\mathrm{d}I/\mathrm{d}V$ maps recorded at the biases corresponding to these three peak energies reveal the characteristic lobe features predominately located at both zigzag edges, demonstrating reproducible patterns in the DFT-calculated local density of states (LDOS) maps of each of the frontier band states (Fig. 3d–f).

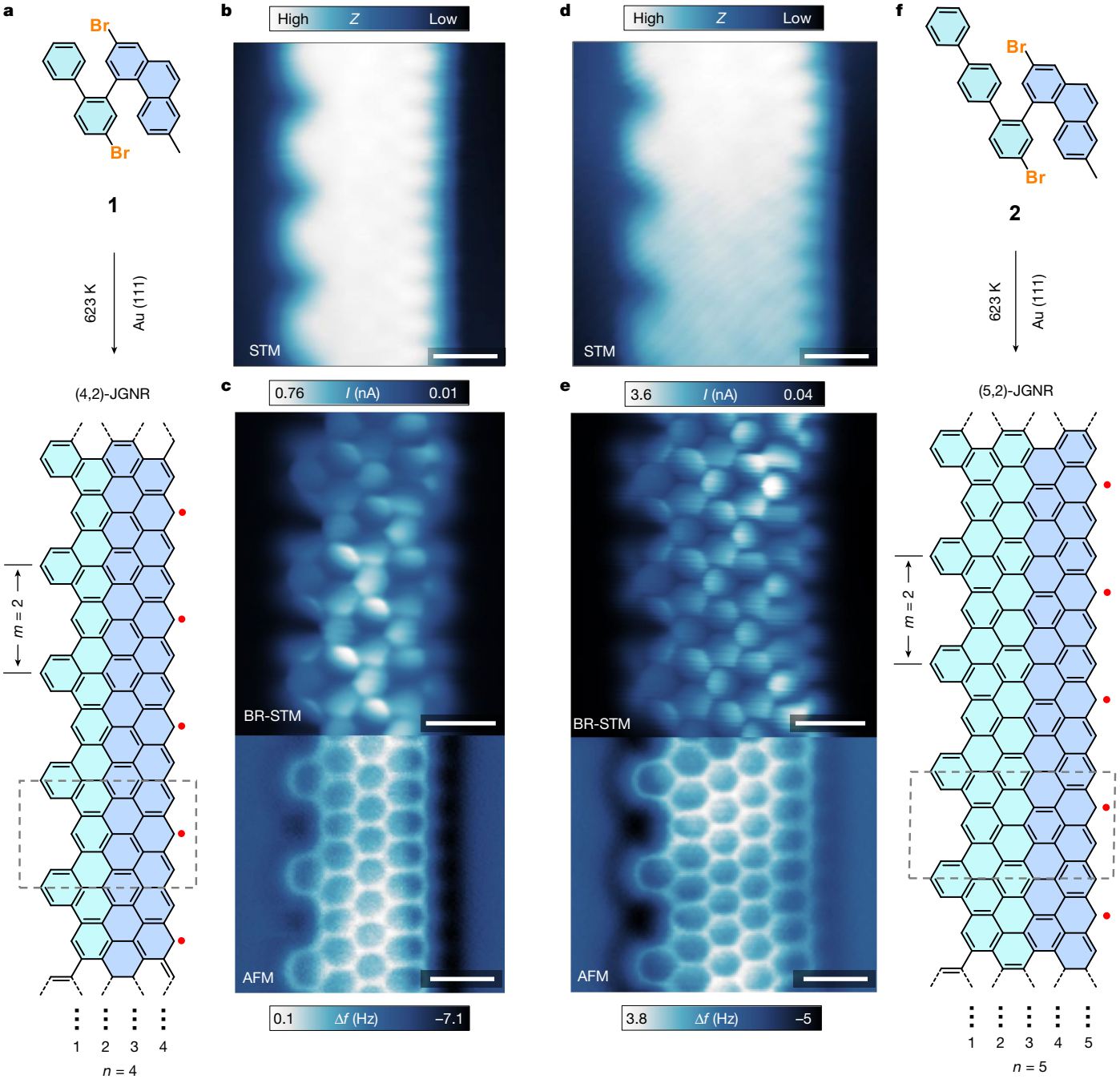

Fig. 2 | On-surface synthesis and structural characterization of the JGNRs. **a**, On-surface synthetic strategy of (4,2)-JGNR. **b**, Constant-current STM image of (4,2)-JGNR (V_s = −800 mV, I_t = 200 pA; where V_s is the sample bias, and I_t is the tunnelling current). **c**, BR-STM image (V_s = −10 mV) and nc-AFM image (V_s = 10 mV) of (4,2)-JGNR acquired at constant-height mode using a qPlus sensor with a CO-functionalized tip. **d**, Constant-current STM image of (5,2)-JGNR (V_s = −800 mV, I_t = 200 pA). **e**, BR-STM image (V_s = −10 mV) and nc-AFM image (V_s = 10 mV) of the (5,2)-JGNR acquired at constant-height mode using a qPlus sensor with a CO-functionalized tip. **f**, On-surface synthetic strategy of (5,2)-JGNR. Scale bars, 5 Å (**b**–**e**).

As shown in Fig. 4a, the d*I*/d*V* spectrum taken over the zigzag edge of (4,2)-JGNR also shows 3 noticeable features, located at 581 ± 19 mV (peak A), 45 ± 5 mV (peak B) and −487 ± 14 mV (peak C), which yields an apparent bandgap of ΔE_{exp} = 536 ± 9 meV. However, peaks A and C are absent in the d*I*/d*V* curve taken over the TDZ edge (Extended Data Fig. 4a,b). The most pronounced peak B spans across E_F, which is tentatively assigned as the partially filled top valence band (spin down, defined as the majority spin, and localized mainly along the intact zigzag edge) arising from the charge transfer owing to the work function difference between GNR and Au(111). The d*I*/d*V* image (Fig. 4c) acquired at the energy positions of peak B shows a petal-shaped feature on the zigzag edge and flower-shaped features distributed on the entire backbone of the (4,2)-JGNR. In contrast, the spatial distribution of the other two peaks of the (4,2)-JGNRs shows similar characteristic zigzag lobe features predominately or exclusively located at the intact zigzag edges for peak A and peak C, respectively (Fig. 4b,d and Extended Data Fig. 5). Similarly (Fig. 4j), the d*I*/d*V* spectrum of (5,2)-JGNR also shows 3 peaks centred at 410 ± 11 mV (peak A), 16 ± 2 mV (peak B) and −510 ± 14 mV (peak C), which yields a smaller bandgap of ΔE_{exp} = 394 ± 9 meV. Compared with (4,2)-JGNR, all the states observed in (5,2)-JGNR experience a slight downwards shift in energy, but show a similar spatial distribution of d*I*/d*V* maps (Fig. 4k–m and Extended Data Fig. 6).

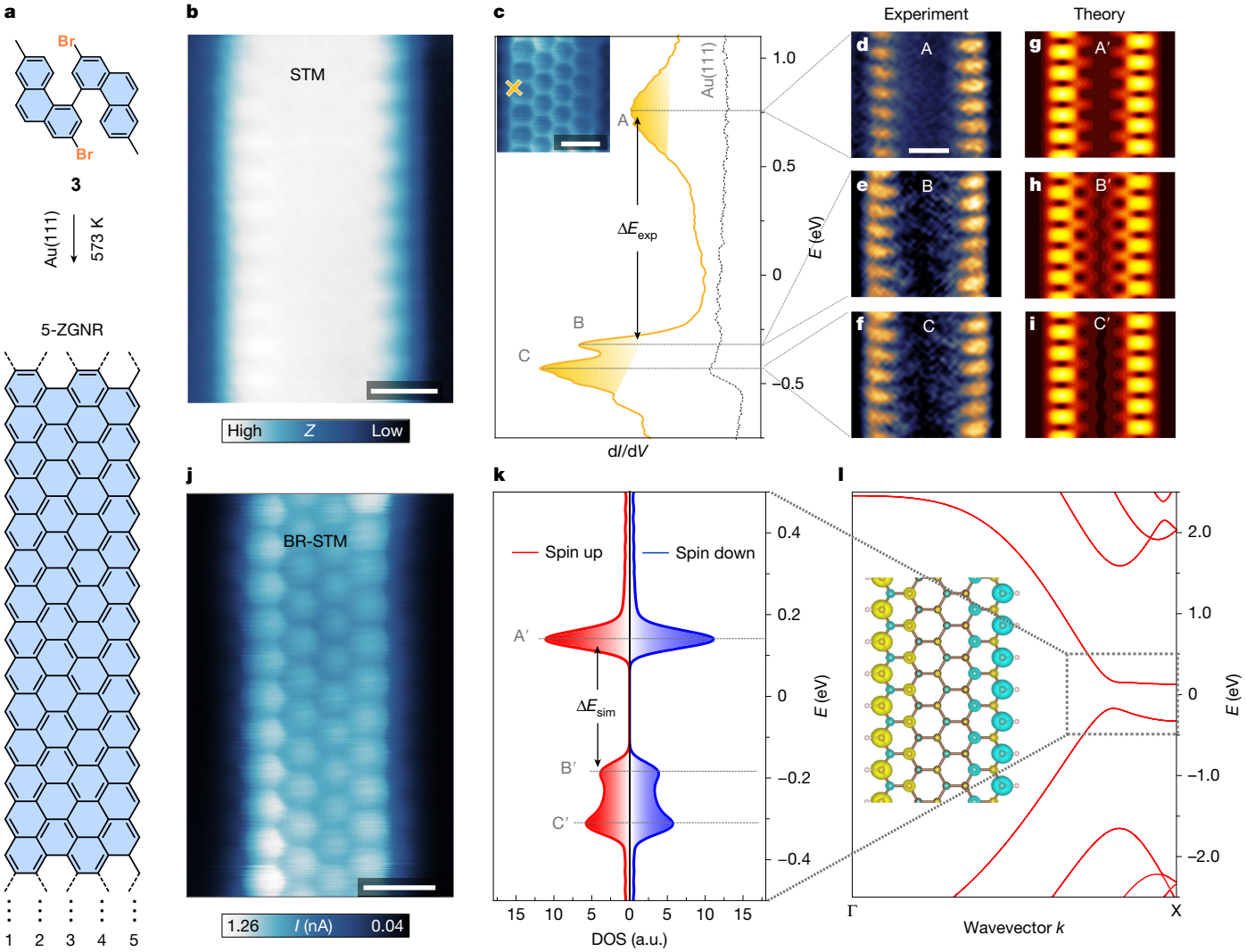

Fig. 3 | Fabrication and characterization of 5-ZGNR. a, On-surface synthetic strategy of 5-ZGNRs. **b**, Constant-current STM image of the 5-ZGNR (V_s = −800 mV, I_t = 200 pA) **c**, dI/dV point spectroscopy of 5-ZGNR on Au(111) at the position marked in the inset panel (red cross). The dashed line shows the Au(111) reference spectrum (modulation voltage V_{ac} = 20 mV). Inset: nc-AFM image acquired at constant-height mode using a qPlus sensor with a CO-functionalized tip (V_s = 10 mV). **d**–**f**, Constant-current dI/dV map recorded at a voltage bias of +750 mV (**d**), −225 mV (**e**) and −470 mV (**f**). V_{ac} = 10 mV. It is noted that the slight asymmetry in the dI/dV maps of the edge states presumably arose from tip asymmetry. **g**–**i**, DFT-calculated LDOS at the energetic positions of A′ (**g**), B′ (**h**) and C′ (**i**) of the DOS spectrum, as marked in **k**. The LDOS are computed at a height of 4 Å above the atomic plane of the 5-ZGNR. **j**, BR-STM image of 5-ZGNR (V_s = 10 mV). **k**, DFT-calculated DOS of spin up (red) and spin down (blue) of a free-standing 5-ZGNR (broadened by 27 meV Gaussian) shows a simulated energy gap (ΔE_{sim}) of 330 meV. **l**, The DFT-calculated band structure of a free-standing 5-ZGNR. Inset: the calculated spin density distribution. Scale bars, 5 Å (**b**–**d**,**j**).

Ab initio calculation of GNRs

Our DFT calculation results on free-standing 5-ZGNRs and two JGNRs offer quantitative evidence that the GNRs synthesized on Au(111) maintain their intrinsic magnetic edge states. Figure 3g–i shows the calculated LDOS maps acquired at the energies corresponding to peak A′ (conduction band minimum), peak B′ (valence band maximum) and peak C′ (the valence band states near the X point) of the free-standing 5-ZGNR, respectively. The distinctive pattern and relative contrast of protrusions lining the edges of 5-ZGNRs observed in experimental dI/dV images (Fig. 3d–f) are well reproduced in the corresponding LDOS maps (Fig. 3g–i). The DFT-calculated band structure (Fig. 3l) reveals that the valence band is more dispersive than the conduction band in the region of around one-third of the Brillouin zone edge near the X point, forming a double-peak structure in the DOS spectrum owing to the van Hove singularities at the valence band maximum away from X (peak B′) and at the X point (peak C′). In contrast, the bottom of the conduction band is significantly flattened in this region of the Brillouin zone, forming only one peak in the DOS (peak A′). Similar behaviour in electronic band dispersion has been observed in 6-ZGNR in a previous study[3]. It is also noted that the experimental gap (980 ± 35 meV) derived from dI/dV spectra is larger than that of the DFT-calculated one (330 meV). Given the tendency of DFT to significantly underestimate quasiparticle bandgaps[44] even when factoring in the screening effects of the underlying gold substrate, it is not surprising that the DFT value is smaller than the experimentally observed gap. Our ab initio calculations on 5-ZGNR reveal that an antiferromagnetic alignment of spins across the ribbon width between ferromagnetically ordered edge states is favoured over both the non-magnetic or a fully ferromagnetic configurations, as illustrated in the spin density plot (the inset of Fig. 3l).

In contrast, our DFT calculations show that the ground state for both the JGNRs studied is ferromagnetic, with ferromagnetic spin-ordered edge states located at only the intact zigzag edge (insets

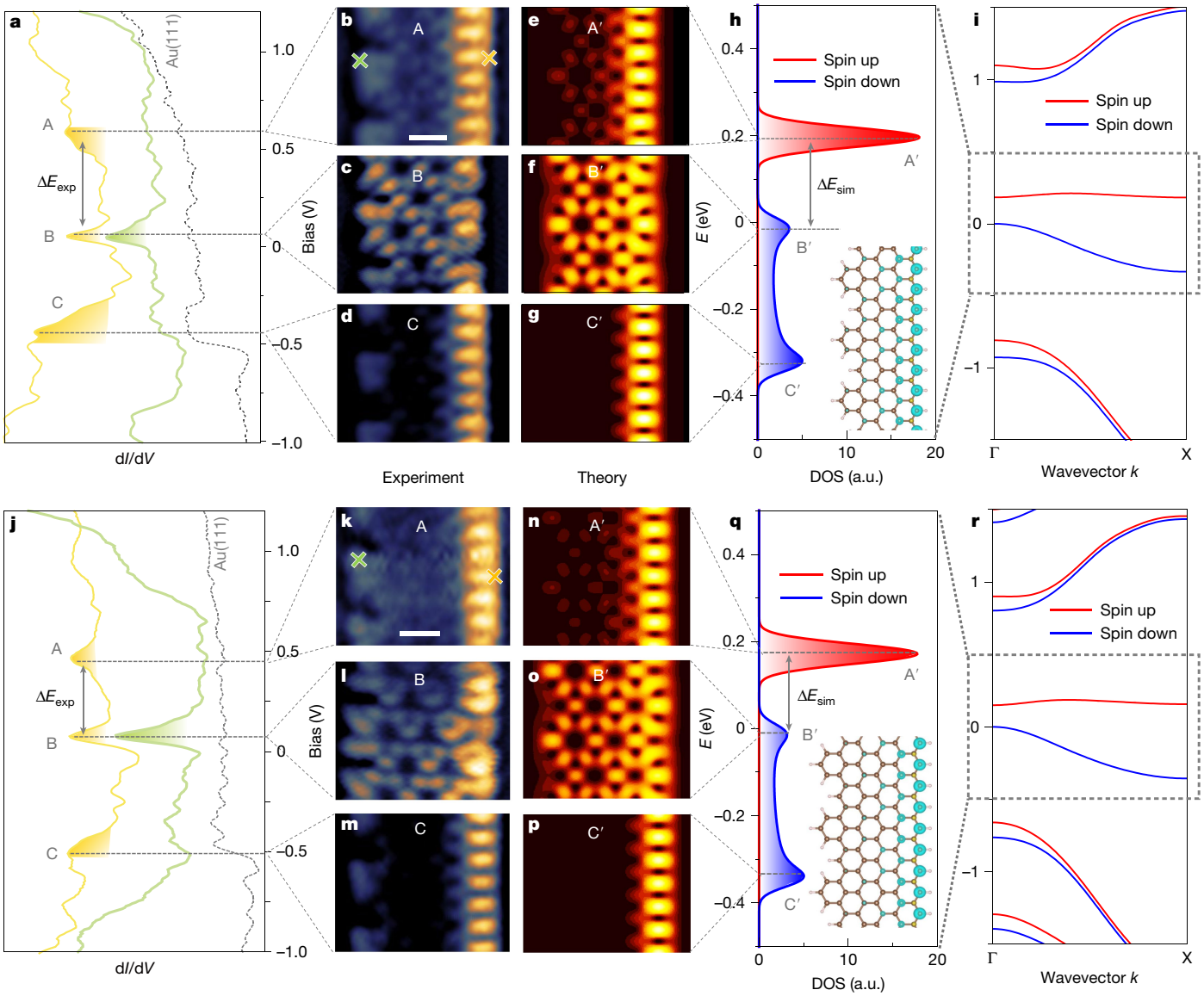

Fig. 4 | Electronic structure of JGNRs. a, d*I*/d*V* point spectroscopy of (4,2)-JGNR on Au(111) at the corresponding coloured position marked in **b** (yellow and green crosses). The dashed line shows the Au(111) reference spectrum (V_{ac} = 20 mV). **b**–**d**, Constant-current d*I*/d*V* maps recorded at the energy positions of A (**b**), B (**c**) and C (**d**) in **a** (V_{ac} = 10 mV). **e**–**g**, DFT-calculated LDOS at the energetic positions of A′ (**e**), B′ (**f**) and C′ (**g**) marked in **h**. The LDOS are computed at a height of 4 Å above the atomic plane of the (4,2)-JGNR. **h**, DFT-calculated DOS of spin up (red) and spin down (blue) of a free-standing (4,2)-JGNR (broadened by 27 meV Gaussian). Inset: the calculated spin density distribution. **i**, The DFT-calculated band structure for a free-standing (4,2)-JGNR. **j**, d*I*/d*V* point spectroscopy of (5,2)-JGNR on Au(111) at the corresponding coloured position marked in **k** (yellow and green crosses). The dashed line shows the Au(111) reference spectrum (V_{ac} = 20 mV). **k**–**m**, Constant-current d*I*/d*V* maps recorded at the energy positions of A (**k**), B (**l**) and C (**m**) in **j** (V_{ac} = 10 mV). **n**–**p**. Calculated DFT LDOS at the energetic positions of A′ (**n**), B′ (**o**) and C′ (**p**) marked in **q**. The LDOS are computed at a height of 4 Å above the atomic plane of a free-standing (5,2)-JGNR. **q**, Calculated DFT DOS of spin up (red) and spin down (blue) of (5,2)-JGNR. Inset: the calculated spin density distribution. **r**, The DFT-calculated band structure of a free-standing (5,2)-JGNR. Scale bars, 5 Å (**b**,**k**).

in Fig. 4h,q). As seen in Fig. 4i,r, each of the originally doubly occupied spin degenerate bands (in spin-unpolarized calculation) splits into a pair of non-degenerate bands with opposite spin orientation. In particular, near zero energy, the two split bands (the lowest conduction band and the highest valence band) bracketing the E_F are edge-state bands and show a splitting energy gap of 0.21 eV and 0.19 eV for the (4,2)-JGNR and (5,2)-JGNR, respectively. Similar to the 5-ZGNR, the highest valence band of both JGNRs is more dispersive than the lowest conduction band (which both are now non-degenerate), forming a double-peak feature (B′ and C′) in the DOS spectrum from the van Hove singularities at the Γ and the X points of the Brillouin zone of the JGNR. Conversely, the first conduction band is notably flattened, forming a sharp peak (A′) in the DOS. Despite variations in the ribbon widths, the calculated LDOS patterns of these peak states remain similar, and correspond well with the experimental d*I*/d*V* maps. As the physical properties of JGNRs near the E_F are dominated by these edge states, variations in the width of the JGNR would only quantitatively change the low-energy physics.

Online content

Any methods, additional references, Nature Portfolio reporting summaries, source data, extended data, supplementary information, acknowledgements, peer review information; details of author contributions and competing interests; and statements of data and code availability are available at https://doi.org/10.1038/s41586-024-08296-x.

1. Ruffieux, P. et al. On-surface synthesis of graphene nanoribbons with zigzag edge topology. *Nature* **531**, 489–492 (2016).
2. Blackwell, R. E. et al. Spin splitting of dopant edge state in magnetic zigzag graphene nanoribbons. *Nature* **600**, 647–652 (2021).
3. Slota, M. et al. Magnetic edge states and coherent manipulation of graphene nanoribbons. *Nature* **557**, 691–695 (2018).
4. Lawrence, J. et al. Probing the magnetism of topological end states in 5-armchair graphene nanoribbons. *ACS Nano* **14**, 4499–4508 (2020).
5. Fujita, M., Wakabayashi, K., Nakada, K. & Kusakabe, K. Peculiar localized state at zigzag graphite edge. *J. Phys. Soc. Jpn* **65**, 1920–1923 (1996).
6. Yang, L., Park, C.-H., Son, Y.-W., Cohen, M. L. & Louie, S. G. Quasiparticle energies and band gaps in graphene nanoribbons. *Phys. Rev. Lett.* **99**, 186801 (2007).
7. de Oteyza, D. G. & Frederiksen, T. Carbon-based nanostructures as a versatile platform for tunable π-magnetism. *J. Phys. Condens. Matter* **34**, 443001 (2022).
8. Yazyev, O. V. & Katsnelson, M. Magnetic correlations at graphene edges: basis for novel spintronics devices. *Phys. Rev. Lett.* **100**, 047209 (2008).
9. Magda, G. Z. et al. Room-temperature magnetic order on zigzag edges of narrow graphene nanoribbons. *Nature* **514**, 608–611 (2014).
10. Son, Y.-W., Cohen, M. L. & Louie, S. G. Half-metallic graphene nanoribbons. *Nature* **444**, 347–349 (2006).
11. Haldane, F. Excitation spectrum of a generalised Heisenberg ferromagnetic spin chain with arbitrary spin. *J. Phys. C* **15**, L1309 (1982).
12. Trauzettel, B., Bulaev, D. V., Loss, D. & Burkard, G. Spin qubits in graphene quantum dots. *Nat. Phys.* **3**, 192–196 (2007).
13. Wang, H. et al. Graphene nanoribbons for quantum electronics. *Nat. Rev. Phys.* **3**, 791–802 (2021).
14. Lieb, E. H. Two theorems on the Hubbard model. *Phys. Rev. Lett.* **62**, 1201 (1989).
15. Cao, T., Zhao, F. & Louie, S. G. Topological phases in graphene nanoribbons: junction states, spin centers, and quantum spin chains. *Phys. Rev. Lett.* **119**, 076401 (2017).
16. Jiang, J. & Louie, S. G. Topology classification using chiral symmetry and spin correlations in graphene nanoribbons. *Nano Lett.* **21**, 197–202 (2020).
17. Hu, J., Zhou, S., Sun, Y., Fang, X. & Wu, L. Fabrication, properties and applications of Janus particles. *Chem. Soc. Rev.* **41**, 4356–4378 (2012).
18. Li, R., Cheng, Y. & Huang, W. Recent progress of Janus 2D transition metal chalcogenides: from theory to experiments. *Small* **14**, 1802091 (2018).
19. Zhang, L. et al. Janus graphene from asymmetric two-dimensional chemistry. *Nat. Commun.* **4**, 1443 (2013).
20. Lu, A.-Y. et al. Janus monolayers of transition metal dichalcogenides. *Nat. Nanotechnol.* **12**, 744–749 (2017).
21. Zhang, J. et al. Janus monolayer transition-metal dichalcogenides. *ACS Nano* **11**, 8192–8198 (2017).
22. Zhang, L. et al. Janus two-dimensional transition metal dichalcogenides. *J. Appl. Phys.* **131**, 230902 (2022).
23. Sun, Q. et al. Coupled spin states in armchair graphene nanoribbons with asymmetric zigzag edge extensions. *Nano Lett.* **20**, 6429–6436 (2020).
24. Rizzo, D. J. et al. Inducing metallicity in graphene nanoribbons via zero-mode superlattices. *Science* **369**, 1597–1603 (2020).
25. Zhang, D.-B. & Wei, S.-H. Inhomogeneous strain-induced half-metallicity in bent zigzag graphene nanoribbons. *npj Comput. Mater.* **3**, 32 (2017).
26. Lee, Y.-L., Kim, S., Park, C., Ihm, J. & Son, Y.-W. Controlling half-metallicity of graphene nanoribbons by using a ferroelectric polymer. *ACS Nano* **4**, 1345–1350 (2010).
27. Kan, E.-j, Li, Z., Yang, J. & Hou, J. Half-metallicity in edge-modified zigzag graphene nanoribbons. *J. Am. Chem. Soc.* **130**, 4224–4225 (2008).
28. Adams, D. J. et al. Stable ferromagnetism and doping-induced half-metallicity in asymmetric graphene nanoribbons. *Phys. Rev. B* **85**, 245405 (2012).
29. Ovchinnikov, A. A. Multiplicity of the ground state of large alternant organic molecules with conjugated bonds: (do organic ferromagnetics exist?). *Theor. Chim. Acta* **47**, 297–304 (1978).
30. Ugeda, M. M., Brihuega, I., Guinea, F. & Gómez-Rodríguez, J. M. Missing atom as a source of carbon magnetism. *Phys. Rev. Lett.* **104**, 096804 (2010).
31. Palacios, J. J., Fernández-Rossier, J. & Brey, L. Vacancy-induced magnetism in graphene and graphene ribbons. *Phys. Rev. B* **77**, 195428 (2008).
32. Song, S. et al. On-surface synthesis of graphene nanostructures with π-magnetism. *Chem. Soc. Rev.* **50**, 3238–3262 (2021).
33. Sakaguchi, H., Song, S., Kojima, T. & Nakae, T. Homochiral polymerization-driven selective growth of graphene nanoribbons. *Nat. Chem.* **9**, 57–63 (2017).
34. Kojima, T. et al. Vectorial on-surface synthesis of polar 2D polymer crystals. *Adv. Mater. Interfaces* **10**, 2300214 (2023).
35. Kojima, T. et al. Molecular-vapor-assisted low-temperature growth of graphene nanoribbons. *J. Phys. Chem. C* **127**, 10541–10549 (2023).
36. Piquero-Zulaica, I. et al. Deceptive orbital confinement at edges and pores of carbon-based 1D and 2D nanoarchitectures. *Nat. Commun.* **15**, 1062 (2024).
37. Li, J. et al. Uncovering the triplet ground state of triangular graphene nanoflakes engineered with atomic precision on a metal surface. *Phys. Rev. Lett.* **124**, 177201 (2020).
38. Li, J. et al. Topological phase transition in chiral graphene nanoribbons: from edge bands to end states. *Nat. Commun.* **12**, 5538 (2021).
39. Kinikar, A. et al. On-surface synthesis of edge-extended zigzag graphene nanoribbons. *Adv. Mater.* **35**, 2306311 (2023).
40. Neaton, J. B., Hybertsen, M. S. & Louie, S. G. Renormalization of molecular electronic levels at metal-molecule interfaces. *Phys. Rev. Lett.* **97**, 216405 (2006).
41. Li, J. et al. Single spin localization and manipulation in graphene open-shell nanostructures. *Nat. Commun.* **10**, 200 (2019).
42. Nguyen, G. D. et al. Atomically precise graphene nanoribbon heterojunctions from a single molecular precursor. *Nat. Nanotechnol.* **12**, 1077–1082 (2017).
43. Chen, Y.-C. et al. Molecular bandgap engineering of bottom-up synthesized graphene nanoribbon heterojunctions. *Nat. Nanotechnol.* **10**, 156–160 (2015).
44. Hybertsen, M. S. & Louie, S. G. Electron correlation in semiconductors and insulators: band gaps and quasiparticle energies. *Phys. Rev. B* **34**, 5390 (1986).

Methods

In-solution and on-surface synthesis

For the synthesis of the precursor of 5-ZGNR, both branches of the Z-shaped precursor are concurrently generated through the Suzuki coupling of 5,5′-dibromo-2,2′-diiodo-1,1′-biphenyl with methylphenyl boronic acid, then generating an ethynyl group via the cleavage of the triisopropylsilyl. Subsequent $PtCl_2$ catalysed cyclization of the ethynyl moiety produces two methylphenanthrene motifs connected by a C–C bond (precursor **3**), serving as branches to construct the zigzag edges. In contrast, for the precursor of JGNRs, one of the two methylphenanthrene branches is substituted by biphenyl and triphenyl groups by an additional step of Suzuki coupling (Extended Data Figs. 7–9). The synthetic procedures of the precursors are detailed in Supplementary Information.

Au(111) single crystal (MaTeck) was cleaned by multiple cycles of Ar^+ sputtering and annealing. A Knudsen cell (MBE-Komponenten) was used for the deposition of precursor molecules onto clean Au(111) surfaces under ultrahigh-vacuum conditions (base pressure, $<2 \times 10^{-10}$ mbar) for on-surface synthesis of product **1**.

The precursor was sublimated at varying temperature for 1 min to achieve a moderate coverage on Au(111). After the deposition of precursors, the sample was stepwise annealed at elevated temperatures as stated in the main text for 20 min to induce polymerization and intramolecular dehydrogenation (Extended Data Fig. 3). The yield of all the GNRs is low under our experimental conditions (Supplementary Figs. 9 and 10), primarily owing to the flexible backbone of the corresponding polymers, which undergo random cyclodehydrogenation reactions during thermal annealing. In addition, the asymmetric precursors **1** and **2** offer limited control over different polymerization modes (Supplementary Fig. 11), namely, head to tail and head to head (or termed as tail to tail)[34,35]. Here we focus on the investigation of the targeted JGNRs through the head-to-tail polymerization.

STM, BR-STM, nc-AFM and d*I*/d*V* characterization

The experiments were conducted in Scienta Omicron LT-STM/AFM systems operated under ultrahigh vacuum (base pressure, $<2 \times 10^{-11}$ mbar) at a temperature of 4.5 K. All the BR-STM and nc-AFM images were taken in constant-height mode with a CO-functionalized tip. A Scienta Omicron microscope was equipped with qPlus sensors S0.8 with a resonance frequency of $f_0 = 39.646$ K Hz, a stiffness of 3,600 N m^{-1} and a quality factor of 119,115. nc-AFM images were collected in a constant-height frequency modulation mode using an oscillation amplitude of 20 pm. The tip–sample distance with respect to an STM set point is indicated in the figure caption for the corresponding AFM image. The images were analysed and processed with Gwyddion software. It is noted that the outer benzene rings on the TDZ edge appear flattened along the ribbon and larger in size than the ones in the backbone, whereas the outer rings at the intact zigzag edges appear stretched in the direction perpendicular to the ribbon. Such a different appearance of hexagons at different edges of JGNRs is presumably owing to varying degrees of CO-tip bending effect due to different edge topologies (Supplementary Fig. 12).

The d*I*/d*V* spectra were collected using a standard lock-in technique with a modulated frequency of 479 Hz. The modulation voltages for individual measurements are provided in the corresponding figure captions. The STM tip was calibrated spectroscopically against the surface state of Au(111) substrate.

Topological classifications and edge-state counting

The *Z* index of the AGNRs, with specific widths and end terminations, has been shown to have an explicit form[16]. This involves simply counting the number of unconnected carbon pairs and the total number of carbon pairs in the unit cell of the AGNR that is commensurate with its end (as shown by the area enclosed by the orange dashed line in Extended Data Fig. 1), given by equation (1).

When considering the edges of a JGNR (which includes a TDZ edge and a regular zigzag edge), we can always find an associated wide AGNR whose end matches the edge of the JGNR (as illustrated in Extended Data Fig. 1). This mapping enables us to calculate the number of edge states at either edge of the JGNR by calculating the number of end states of the corresponding AGNR.

In Extended Data Fig. 1, each unit cell of the JGNR is enclosed by two grey dotted lines and the unit cells are labelled 1, 2, 3, …, *L*, with a total of *L* unit cells of a finite-length ribbon (it is noted that the unit cell of JGNR is different from that of AGNR). In mapping the edge of JGNR to the end of a wide AGNR, the corresponding AGNR contains *L* repeat units along its width direction. This means that *W*, the width of the wide AGNR, equals *L* times the width of each repeat unit, and W_{notco} equals *L* times the number of the not-connected carbon pair in each repeat unit. With this correspondence, we are able to perform detailed edge-state counting for different edges.

First, we map the edge of the ZGNR/JGNR to the end of a wide AGNR. Extended Data Fig. 2a–d shows the corresponding wide AGNR for the $m = 1$ TDZ edge, $m = 2$ TDZ edge, $m = 3$ TDZ edge and a regular zigzag edge, respectively, for the large-*L* limit. Next, we applied equation (1) to compute the *Z* index. The detailed calculations of *Z* for the TDZ and pristine edge of certain finite-length JGNRs, when considered as the ends of wide AGNRs, are as follows.

(1) For the case where the distance between additional benzene rings on the TDZ edge is $m = 1$, as shown in Extended Data Fig. 2a, and there are *L* additional benzene rings in the JNGR, the number of unconnected carbon pairs is *L* and the number of connected carbon pairs is 3*L* in the unit cell of the corresponding wide AGNR. The total number of rows of carbon atoms forming the AGNR width is 4*L*, and $Z = L - \frac{4L}{3} = -\frac{1}{3}L$ for the unit cell.

(2) For the case where the distance between additional benzene rings on the TDZ edge is $m = 2$, as shown in Extended Data Fig. 2b, the number of unconnected carbon pairs is 2*L* and the number of connected carbon pairs is 4*L*. The total number of rows of carbon atoms forming the AGNR width is 6*L* and $Z = 2L - \frac{6L}{3} = 0$ for the unit cell. That means no edge states for the TDZ edge in this case.

(3) For the case where the distance between additional benzene rings on the TDZ edge is $m = 3$, as shown in Extended Data Fig. 2c, the number of unconnected carbon pairs is 3*L* and the number of connected carbon pairs is 5*L*. The total number of rows of carbon atoms is 8*L* and $Z = 3L - \frac{8L}{3} = \frac{1}{3}L$ in the unit cell.

(4) For a regular zigzag edge, as shown in Extended Data Fig. 2d, the number of unconnected carbon pairs is 1 per benzene ring and the number of connected carbon pairs is 1 per benzene ring. The total number of rows of carbon atoms forming the AGNR width is 2 per benzene ring and Z/(number of benzene rings) $= 1 - \frac{2}{3} = \frac{1}{3}$ per benzene ring. We note that for an AGNR unit cell containing *L* benzene rings at the regular zigzag edge end, the corresponding CPI is $Z = \frac{1}{3}L$.

Computational method and analyses

First-principles DFT calculations within the local spin density approximation were performed using the Quantum ESPRESSO package[45,46]. A supercell geometry was employed, with a 10-Å vacuum spacing placed in all non-periodic directions to prevent interaction between replicas. The atomic geometry was fully relaxed until all components of the forces on each atom were smaller than 0.01 eV $Å^{-1}$. A 100-Rydberg wavefunction energy cut-off, along with scalar relativistic and norm-conserving pseudopotentials for C and H, were used[47,48].

In understanding the localization of the edge states in (n,$m = 2$)-JGNRs, previous tight-binding calculations on infinite-width pristine ZGNRs indicate a reciprocal vector *k*-dependent localization length at the zigzag edge, with states being more localized when closer to the X point of the ZGNR Brillouin zone[5]. As the edge states of (n,$m = 2$)-JGNRs can be viewed as band-folded states of ZGNR, for the peak originating from

states near the X point of the highest valence band of JGNR (peak C′), they all originate from states near the X point of the pristine ZGNR. The localization length of those states is small compared with the width of the JGNRs, so the theoretical LDOS pattern shows a localized pattern at the zigzag edge (Fig. 4g,p). In contrast, for states more towards to the Γ point (at near 1/3 way from X to Γ or beyond), the localization length of those states in the infinite-width pristine ZGNRs exceeds the width of the JGNRs considered. The corresponding theoretical LDOS pattern (peak B′) shows a delocalized pattern throughout the ribbon width (Fig. 4f,o). For the peak formed by the conduction band (peak A′), it comprises states from the entire JGNR Brillouin zone, and the LDOS pattern can be viewed as a mixture of the previous two patterns (Fig. 4e,n).

We note also that in the experiment, peak B is located near E_F for both JGNRs. This is owing to the fact that the work function difference between our GNRs (about 4.5 eV) and the Au(111) substrate (about 5.3 eV) entails a charge transfer from the JGNRs to the substrate, which lifts the valence band maximum upwards to the Fermi level. By performing calculations at different doping levels, we estimate the charge transfer to be approximately 0.1 holes per JGNR unit cell and demonstrate that the localized spin-polarized edge states remain stable under this amount of charge transfer (Supplementary Figs. 3–5). Moreover, calculations on the non-magnetic phase at various doping levels show that not only is the energy of the non-magnetic phase higher than that of the ferromagnetic phase at the same doping level but also the calculated DOS and LDOS do not match our experimental results (Supplementary Figs. 6–8).

Data availability

All data are available in the paper or the Supplementary Information. The scanning probe microscopy spectra data and theoretical calculation results are available in the Zenodo repository at https://doi.org/10.5281/zenodo.13894455 (ref. 49).

45. Giannozzi, P. et al. Quantum ESPRESSO: a modular and open-source software project for quantum simulations of materials. *J. Phys. Condens. Matter* **21**, 395502 (2009).
46. Giannozzi, P. et al. Advanced capabilities for materials modelling with Quantum ESPRESSO. *J. Phys. Condens. Matter* **29**, 465901 (2017).
47. Hamann, D. Erratum: Optimized norm-conserving vanderbilt pseudopotentials [Phys. Rev. B 88, 085117 (2013)]. *Phys. Rev. B* **95**, 239906 (2017).
48. Van Setten, M. J. et al. The PseudoDojo: training and grading a 85 element optimized norm-conserving pseudopotential table. *Comput. Phys. Commun.* **226**, 39–54 (2018).
49. Song, S. et al. Janus graphene nanoribbons with localized states on a single zigzag edge. *Zenodo* https://doi.org/10.5281/zenodo.13894455 (2024).

Acknowledgements J.L. acknowledges support from the NRF, Prime Minister's Office, Singapore, under the Competitive Research Program Award (NRF-CRP29-2022-0004), MOE grants (MOE T2EP50121-0008 and MOE-T2EP10221-0005) and Agency for Science, Technology and Research (A*STAR) under its AME IRG Grant (Project715 number M21K2c0113). S.G.L. acknowledges the support from the US National Science Foundation under grant number DMR-2325410, which provided all the theoretical topological formulation and analyses as well as the DFT calculations. H.S. acknowledges the support from KAKENHI programme number 22H01891. T.K. acknowledges the support from KAKENHI programme number 23K04521. S.S. acknowledges the support from A*STAR under its AME YIRG Grant (M22K3c0094).

Author contributions J.L. supervised the project and organized the collaboration. S.S. and J.L. conceived and designed the experiments. S.S. and Y.T. carried out the STM and nc-AFM measurements. Z.X., S.S., T.K. and H.S. synthesized the organic precursors. S.G.L. conceived the topological equivalence of the defect edge of JGNR with the end of AGNR, and supervised the theoretical analyses and calculations. W.T., J.R. and Y.H. performed the theoretical studies and DFT calculations. F.J.G. assisted in the optimization of the nc-AFM measurements and instrumentation. W.H. participated in scientific discussion. S.S., W.T., S.G.L. and J.L. wrote the paper with inputs from all authors.

Competing interests F.J.G. holds patents on the qPlus sensor. The other authors declare no competing interests.

Additional information

Supplementary information The online version contains supplementary material available at https://doi.org/10.1038/s41586-024-08296-x.

Correspondence and requests for materials should be addressed to Hiroshi Sakaguchi, Steven G. Louie or Jiong Lu.

Peer review information *Nature* thanks Ashok Keerthi, David Serrate and the other, anonymous, reviewer(s) for their contribution to the peer review of this work.

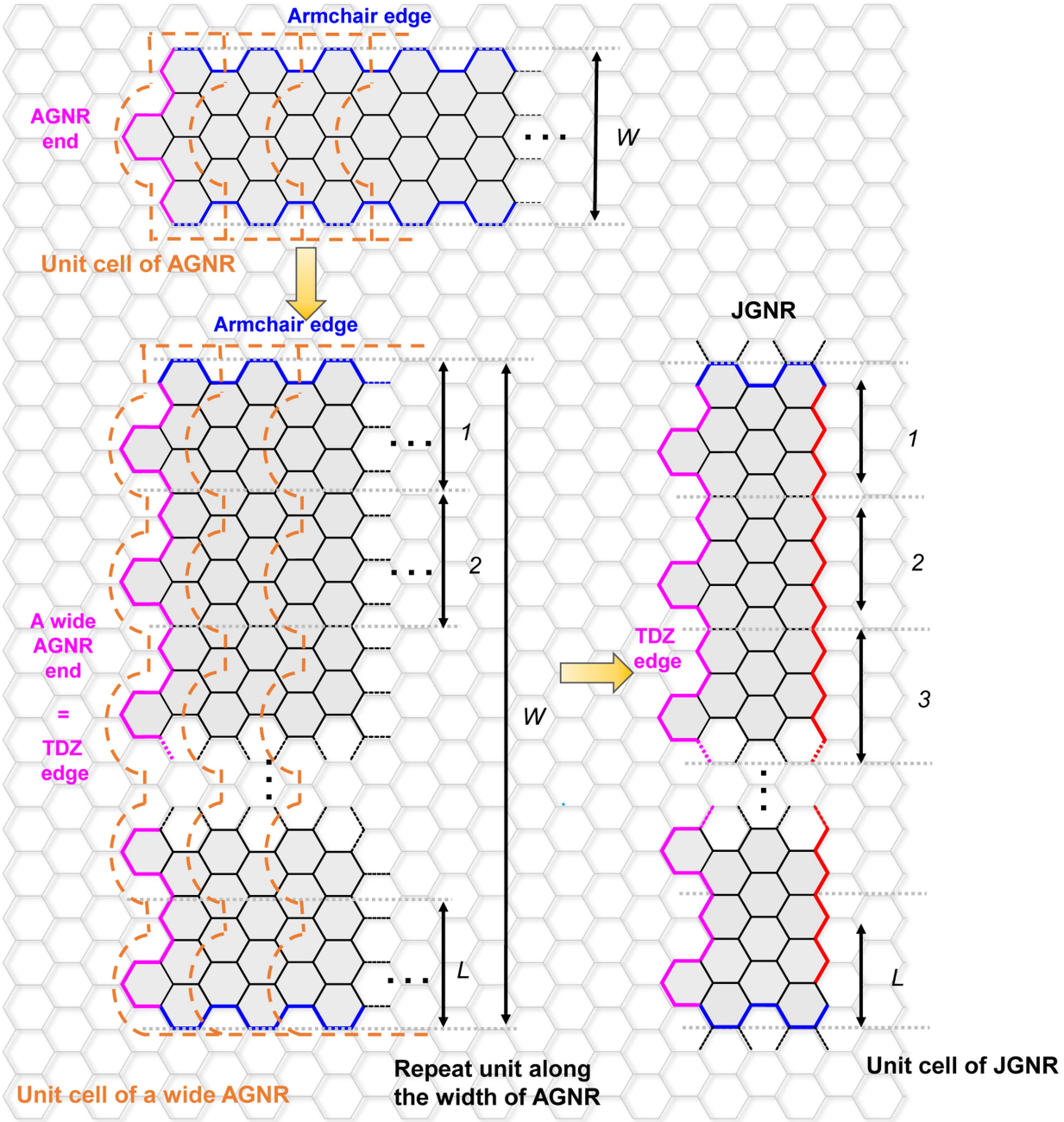

Extended Data Fig. 1 | Schematic illustration of the correspondence between the end of a wide AGNR and the edge of JGNR. The unit cell of the AGNR, commensurate with its termination, is enclosed by an orange dashed curve. The quantities W and W_{notco} in Eq. (1) are to be counted within this specific unit cell. The unit cell of the finite-size JGNR is defined by the area between two grey lines, where 1, 2, ..., L label the unit cells. A sufficiently wide AGNR can always be found that shares the same termination as the edge of the JGNR. Through this mapping, the associated AGNR contains L repeated units along its width direction. The unit cell of the wide AGNR, commensurate with its termination, is the area enclosed by the orange dashed curve.

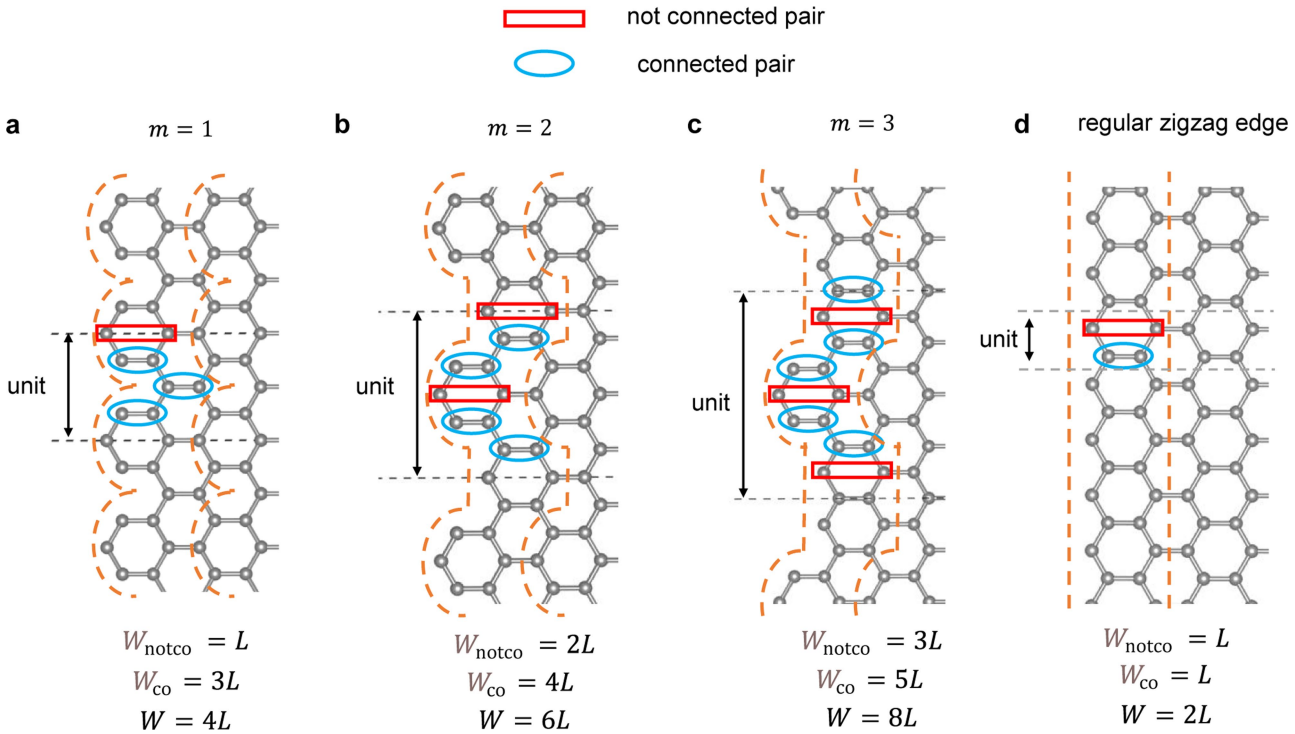

Extended Data Fig. 2 | JGNR edge states counting. Sketch of the defective edge of JGNR with different m value, which is mapped to the end of a large width AGNR with unit cell enclosed by the orange dashed curve that is commensurate with its termination on the left (the topological defect edge of interest). W is the number of carbon rows forming the length of the finite-size JGNR (which is equivalent to the number of carbon rows forming the width of the associated AGNR). W_{co} and W_{notco} are the number of connected and unconnected carbon pairs, respectively, in the unit cell of the wide AGNR. L is the number of repeat units along the width of the associated AGNR direction (i.e., L is number of unit cells forming the length of the finite-size ZGNR of physical interest), and the repeat unit is denoted by the area between the two grey dashed lines. The relationships between L and W, W_{co} and W_{notco} are shown. **a**, A defect edge with $m = 1$. **b**, A defect edge with $m = 2$. **c**, A defect edge with $m = 3$. **d**, A regular zigzag edge. The repeat unit along the width of AGNR direction is a single benzene ring. These quantities are important in the calculation of Z index.

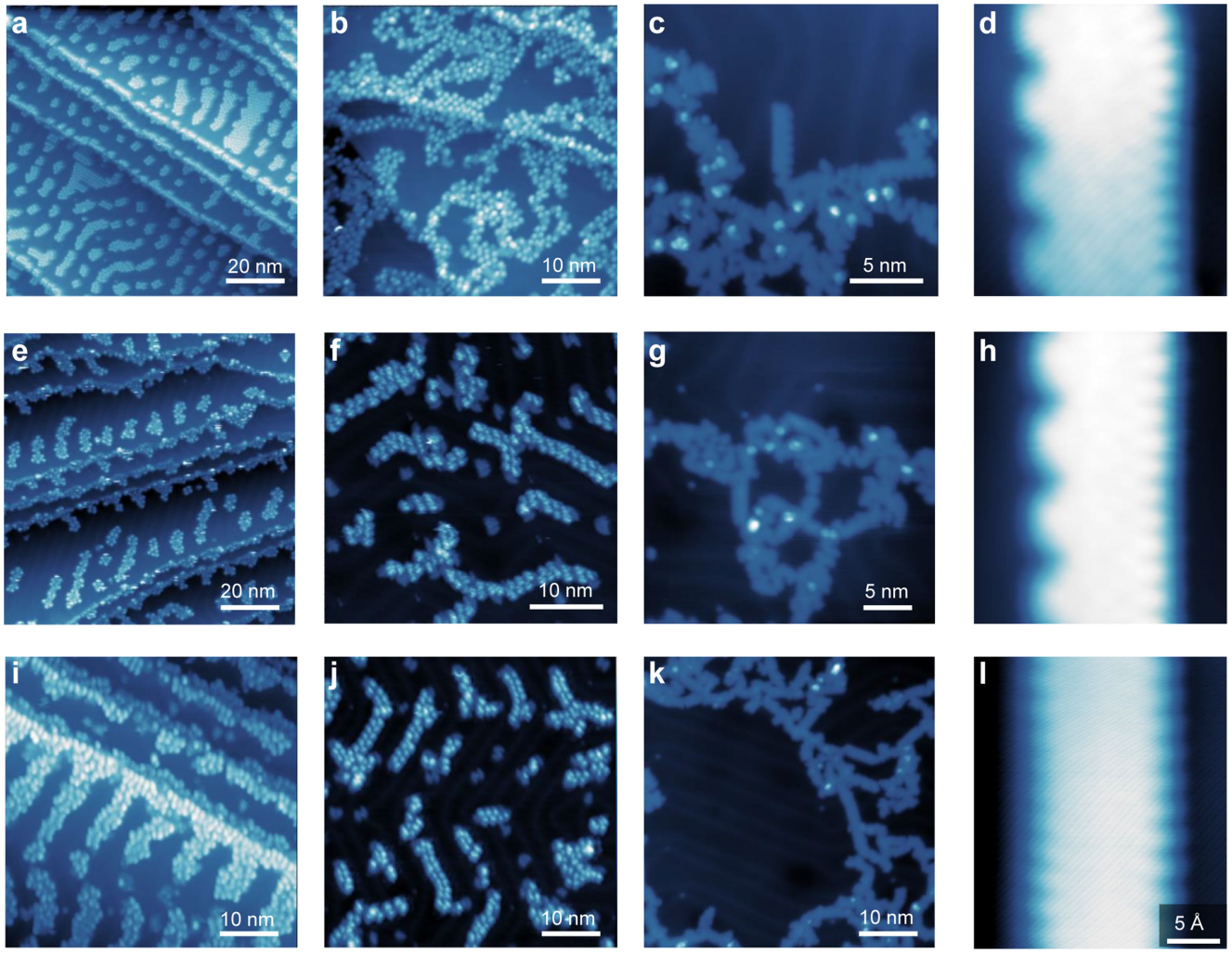

Extended Data Fig. 3 | On-surface synthesis of the 5-ZGNR and JGNRs. **a, e, f.** STM topographic image of molecular precursor **1, 2**, and **3** as deposited on Au(111), respectively. **b, f, j.** The STM topographic images of polymer chains obtained by annealing the sample of **a, e, f** up to 473, 473, and 423 K, respectively. **c, g, k.** STM topographic images of fully cyclized (*5,2*)-JGNR, (*4,2*)-JGNR and 5-ZGNR through a subsequent annealing at 623, 623, and 573 K (V_s = 1 V, I_t = 100 pA), respectively. **d, h, l.** Constant current zoom-in STM images of an individual (*5,2*)-JGNR, (*4,2*)-JGNR and 5-ZGNR, respectively (V_s = −800 mV, I_t = 200 pA, CO-functionalized tip).

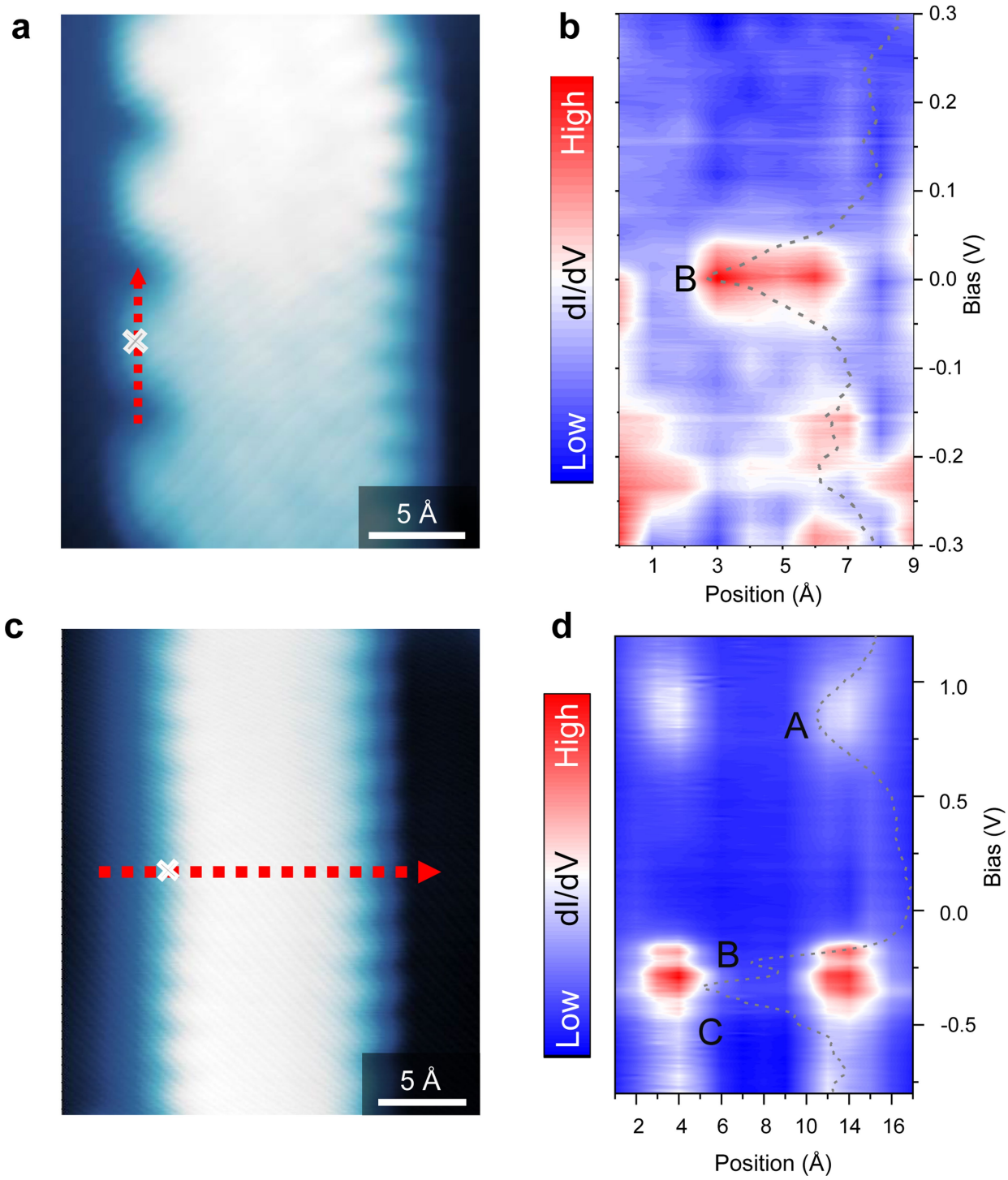

Extended Data Fig. 4 | Spatial localization of edge state of 5-ZGNR and TDZ edge state of (*5,2*)-JGNR. a, Constant current STM images of 5-ZGNR, (V_s = −800 mV, I_t = 200 pA, CO-functionalized tip). **b**, Colour-coded d*I*/d*V* spectra collected as a function of position along the red dotted line (from left to right) in a (V_{ac} = 20 mV, V_s = 1.5 V). The dashed line overlayed on **b** is the point d*I*/d*V* spectrum acquired at the position labelled with a cross in **a**. **c**, Constant current STM images of (*5,2*)-JGNR, (V_s = −800 mV, I_t = 200 pA, CO-functionalized tip). **d**, Colour-coded d*I*/d*V* spectra collected as a function of position along the red dotted line (from top to bottom) in **c** (V_{ac} = 20 mV, V_s = 1.5 V). The dashed line overlayed on **d** is the point d*I*/d*V* spectrum acquired at the position labelled with a cross in **c**.

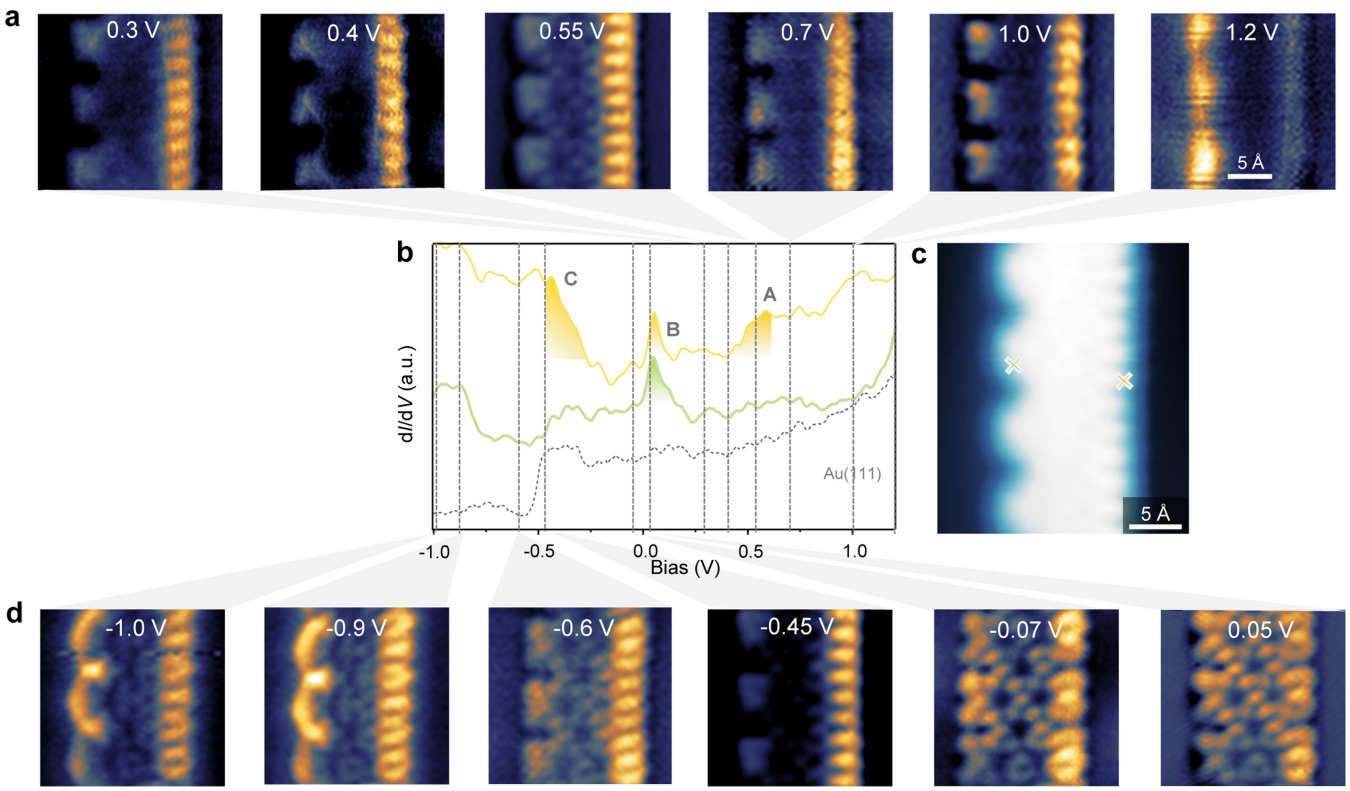

Extended Data Fig. 5 | Bias-dependent d*I*/d*V* maps of (*4,2*)-JGNR across a wide energy window. a, d, Constant-current d*I*/d*V* maps of (*4,2*)-JGNR recorded at various sample biases marked in **b** by the dashed vertical lines (V_{ac} = 10 mV). **b**, d*I*/d*V* point spectrum of (*4,2*)-JGNR on Au(111) acquired at the positions marked in panel **c** (yellow and green cross). Grey dashed line spectrum represents the Au(111) reference spectrum (V_{ac} = 20 mV). **c**, Constant current STM images of (*4,2*)-JGNR, (V_s = 800 mV, I_t = 200 pA, CO-functionalized tip).

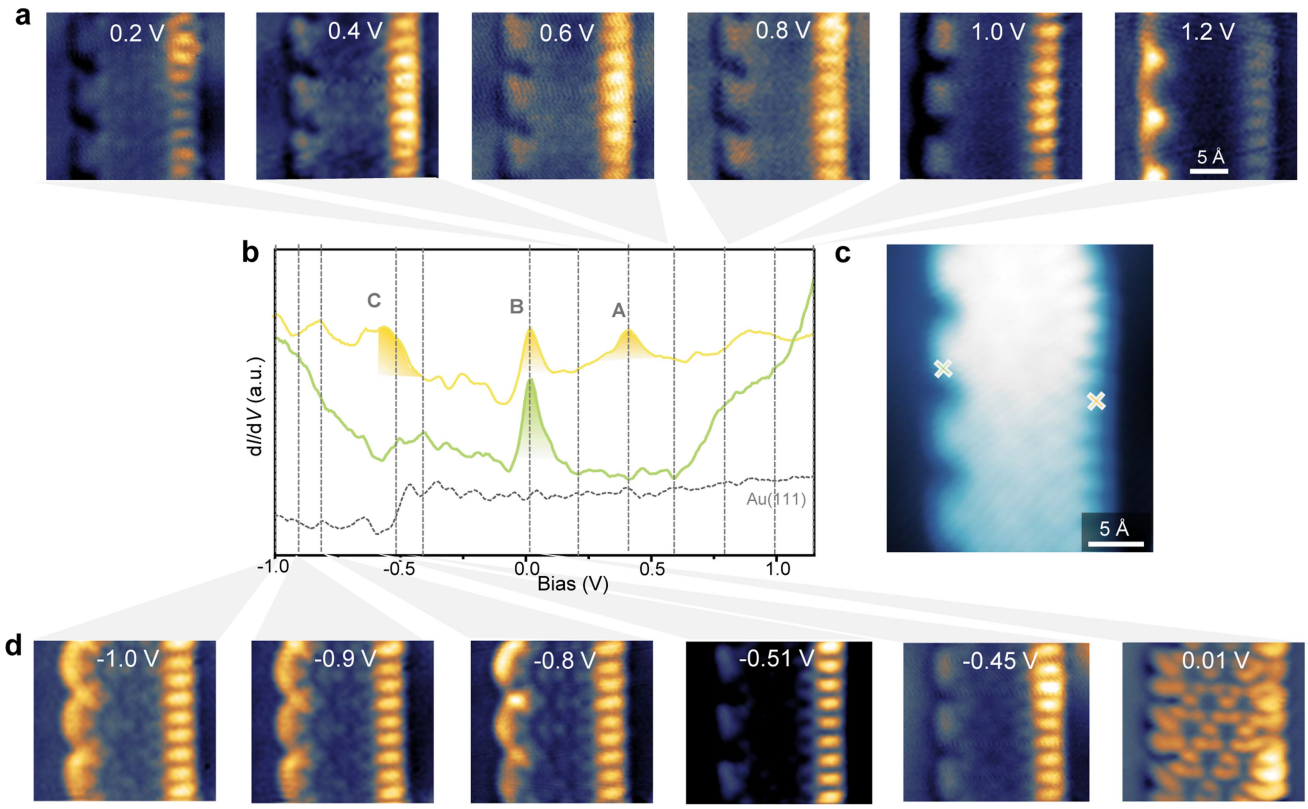

Extended Data Fig. 6 | Bias-dependent d*I*/d*V* maps of (*5,2*)-JGNR across a wide energy window. a, d, Constant-current d*I*/d*V* maps of (*5,2*)-JGNR recorded at various sample biases marked in **b** by the dashed vertical line (V_{ac} = 10 mV). **b**, d*I*/d*V* point spectrum of (*5,2*)-JGNR on Au(111) acquired at the position marked in panel **c** (yellow and green cross). Grey dashed line spectrum represents the Au(111) reference spectrum (V_{ac} = 20 mV). **c**, Constant current STM images of (*5,2*)-JGNR, (V_s = −800 mV, I_t = 200 pA, CO-functionalized tip).

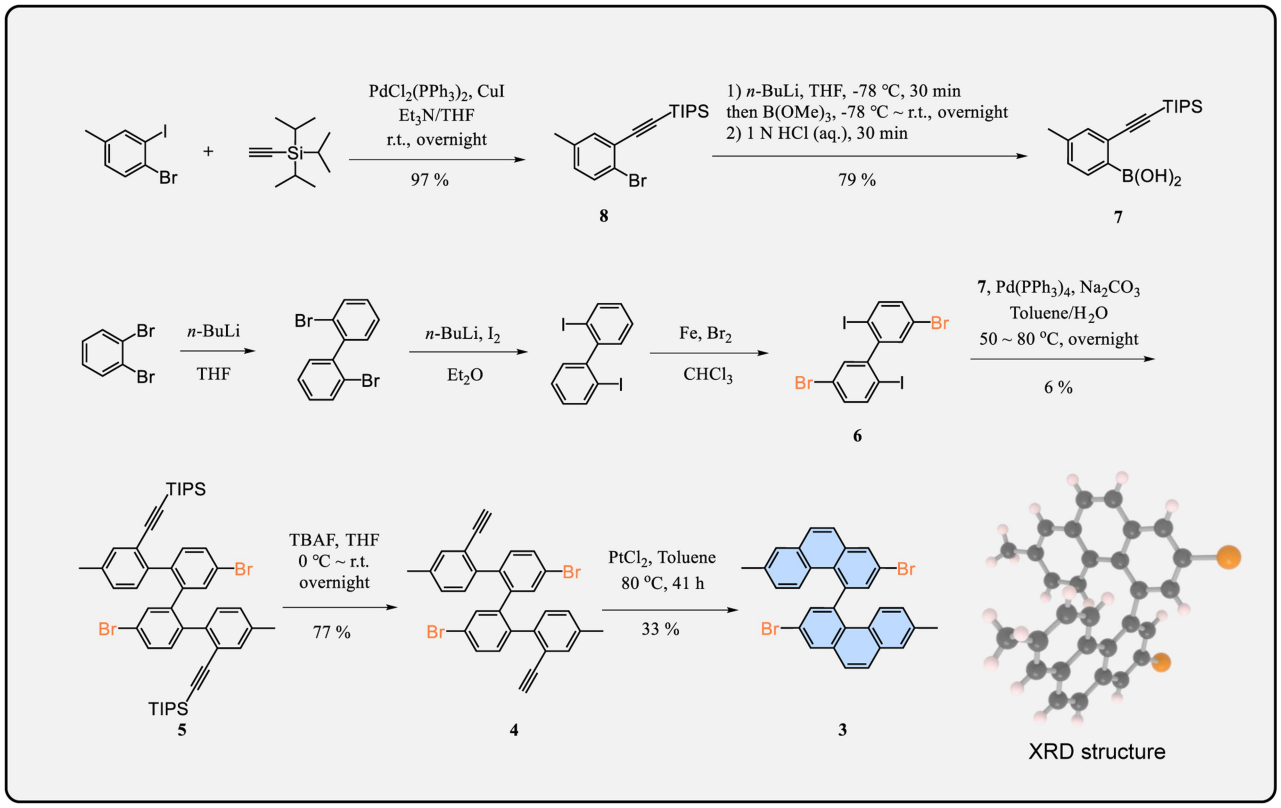

Extended Data Fig. 7 | Symmetric design and synthesis of precursor 3. The synthetic scheme towards the Z-shape backbone by simultaneously constructing the two identical methylphenanthrene branches and its single crystal X-ray diffraction (XRD) structure.

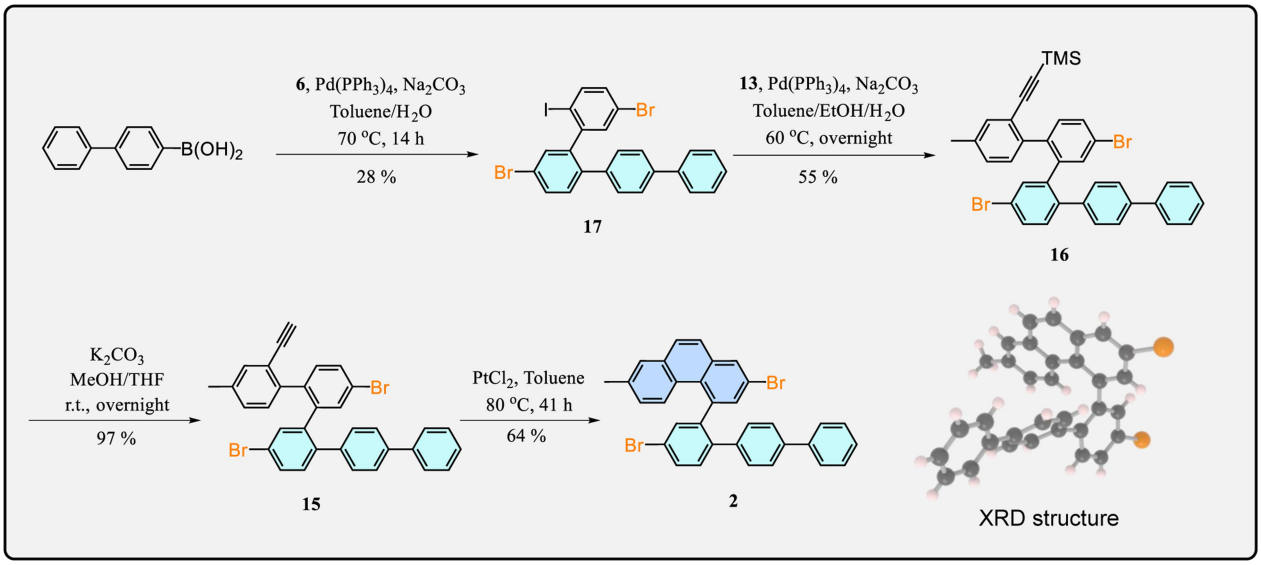

Extended Data Fig. 8 | Asymmetric design and synthesis of precursor 2. The synthetic scheme towards the Z-shape backbone by separately constructing the triphenyl branch and the methylphenanthrene branch of precursor **2** and its single crystal XRD structure.

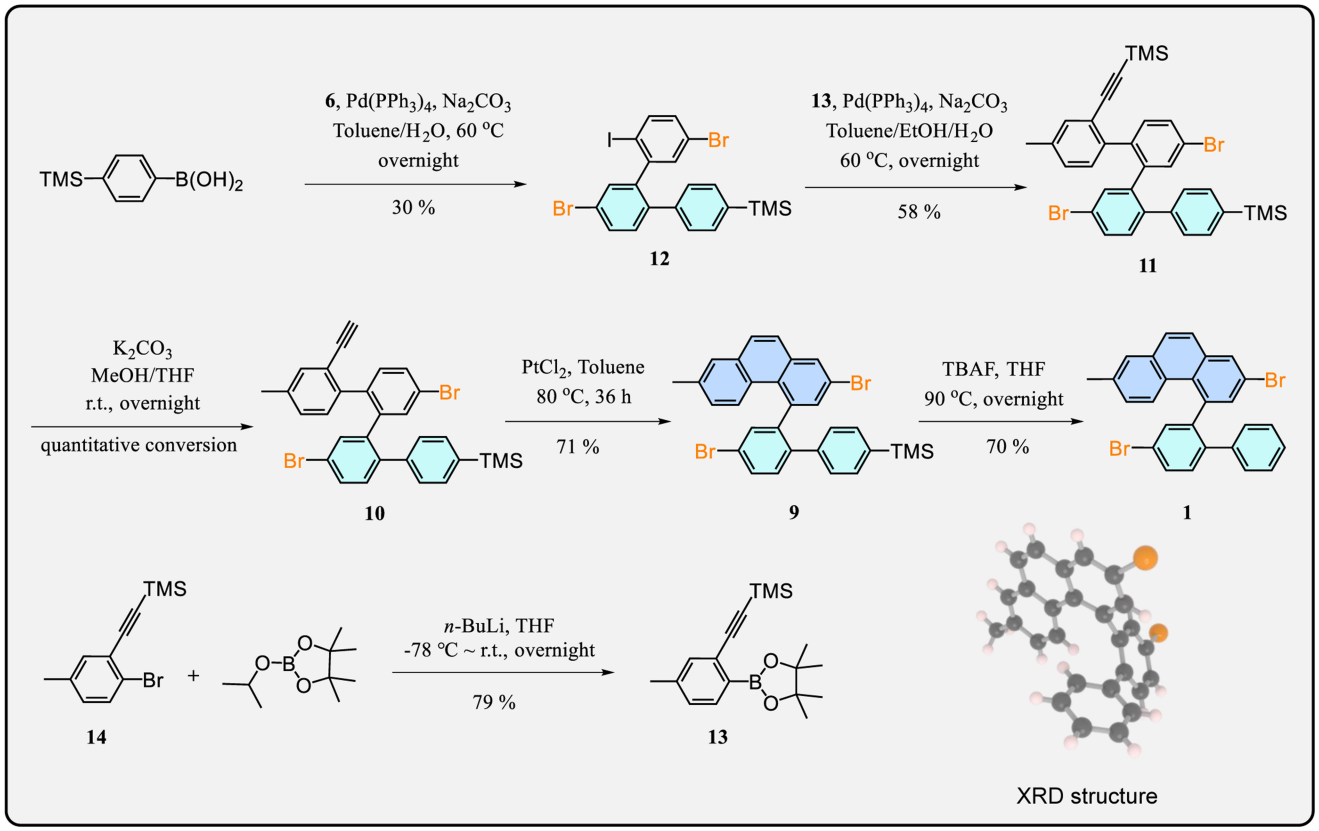

Extended Data Fig. 9 | Asymmetric design and synthesis of precursor 1. The synthetic scheme towards the Z-shape backbone by separately constructing the biphenyl branch and the methylphenanthrene branch of precursor **1** and its single crystal XRD structure.